Accepted Manuscript

Mixed-ligand Cu(II) hydrazone complexes designed to enhance anticancer activity

QingYou Mo, JunGang Deng, Yani Liu, GuiDong Huang, ZuoWen Li, Ping Yu, Yi Gou, Feng Yang

PII: S0223-5234(18)30578-6

DOI: 10.1016/j.ejmech.2018.07.022

Reference: EJMECH 10557

To appear in: *European Journal of Medicinal Chemistry*

Received Date: 17 May 2018

Revised Date: 5 July 2018

Accepted Date: 8 July 2018

Please cite this article as: Q. Mo, J. Deng, Y. Liu, G. Huang, Z. Li, P. Yu, Y. Gou, F. Yang, Mixed-ligand Cu(II) hydrazone complexes designed to enhance anticancer activity, *European Journal of Medicinal Chemistry* (2018), doi: 10.1016/j.ejmech.2018.07.022.

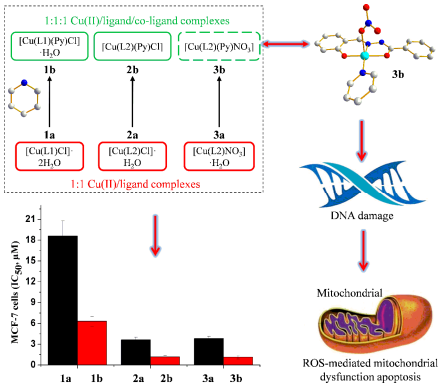

Mixed-ligand Cu(II) hydrazone complexes designed to enhance anticancer activity

QingYou Mo [a,b,1], JunGang Deng[a,1], Yani Liu[c], GuiDong Huang[a], ZuoWen Li[b], Ping Yu[d], Yi Gou[b]*, Feng Yang[d]*

[a] Affiliated hospital, Guilin Medical University, Guilin, Guangxin, China

[b] School of Pharmacy, Nantong University, Nantong, Jiangsu, China

[c] Department of Pharmacy, Union Hospital, Tongji Medical College, Huazhong University of Science and Technology, Wuhan, China

[d] State Key Laboratory for the Chemistry and Molecular Engineering of Medicinal Resources, Ministry of Science and Technology of China, Guangxi Normal University, Guilin, Guangxi, China

*Corresponding authors.

E-mail addresses: sanchuanok@126.com (Y. Gou), fyang@mailbox.gxnu.edu.cn (F. Yang).

[1] These authors have contributed equally to this work.

Abstract

The ligand quantity, ligand type, and coordination geometry have important influences on the anticancer activity of metal-based complexes. On the basis of the structures of previously reported 1:1 Cu(II)/ligand complexes ([Cu(L1)Cl]·$2H_2O$ **1a**, [Cu(L2)Cl]·H_2O **2a**, and [Cu(L2)NO_3]·H_2O **3a**), we subsequently designed, developed, and characterized a series of corresponding 1:1:1 Cu(II)/ligand/co-ligand complexes ([Cu(L1)(Py)Cl]·H_2O **1b**, [Cu(L2)(Py)Cl] **2b**, and [Cu(L2)(Py)NO_3] **3b**), where L1 = (*E*)-*N*′-(2-hydroxybenzylidene)acetohydrazide, L2 = (*E*)-*N*′-(2-hydroxybenzylidene)benzohydrazide, and Py = pyridine. All six Cu(II) complexes were assessed for their in vitro anticancer properties against a panel of human cancer cells, including *cis*platin-resistant A549cisR cell lines. Interestingly, we observed that the 1:1:1 Cu/ligand/co-ligand mixed-ligand Cu(II) complexes exhibited higher anticancer activity than the corresponding 1:1 Cu(II)/ligand complexes. In particular, the 1:1:1 Cu(II)/ligand/co-ligand complex **3b** displayed the greatest toxicity toward several cancer cells with better IC_{50} (1.12–3.77 μM) than *cis*platin. Further mechanistic explorations showed that the **3b** complex induced DNA damage, thus resulting in mitochondria-mediated apoptotic cell death. Furthermore, the **3b** complex displayed pronounced cytostatic effects in the MCF-7 3D spheroid model.

Keywords: Mixed-ligand copper(II) complexes; Anticancer activity; Spheroid assay; Anticancer mechanism

1. Introduction

Although highly effective in treating various solid tumors, platinum-based agents (e.g., *cis*platin and its second and third generation analogs) are still limited by dose-limiting side effects and inherited or acquired drug resistance [1, 2]. These drawbacks have galvanized chemists to discover alternative chemotherapeutic strategies that are based on endogenous metals with improved pharmacological properties [3–6]. Among the bio-essential metals, copper is found in all living organisms and can be employed as a catalytic and structural cofactor; therefore, it has a pivotal role in redox chemistry, development, and growth pathways [7]. Copper has played a central role in angiogenesis, which is a critical process for tumor growth, invasion, and metastasis [8–10]. Many investigations reported that numerous cancerous tissues, such as breast, brain, and prostate cancer tissues, take up more copper than normal tissues [5, 11, 12]. Therefore, copper complexes have been considered promising alternatives to platinum-based agents, and a variety of copper-based anticancer agents have been studied as potential anticancer drugs in recent years [5].

Hydrazones are known to be an important class of Schiff base ligands with many pharmacological activities, such as anticancer, antituberculostatic, and antimicrobial activities [13–15]. Hydrazones can coordinate in either monoanionic, dianionic, or neutral forms and can form various complexes with many transition metal cations, such as Cu(II), Fe(III), and Zn(II) [16–18]. Many investigations demonstrated that the biological activity of hydrazone copper complexes was higher than that of ligands alone; this finding is particularly relevant for anticancer activity [19–23]. The introduction of N-containing co-ligands such as imidazole, pyridine, quinoline, phenanthroline, and their derivatives might affect the planarity, hydrophobicity, and coordination geometry of copper complexes and the anticancer activity of copper-based agents [24, 25]. A large number of mixed-ligand copper complexes were recently reported, and many of them showed prominent anticancer activity [25–33]. These studies provided opportunities for developing copper-based anticancer agents that contain hydrazones ligands and N-containing co-ligands. In addition, pyridine is a common prodrug and is one of the building blocks of many biologically

important molecules. Recently, the application and chemistry of pyridine compounds have attracted significant attention because of their biological importance [34].

The purpose of our study was to explore whether the introduction of an N-containing co-ligand pyridine (Py) into aroylhydrazones copper(II) complexes would result in a synergistic effect and whether this approach could consequently represent an effective strategy for potentially developing copper-based anticancer drugs. Given that 1:1 Cu(II)/ligand complexes ([Cu(L1)Cl]·$2H_2O$ **1a**, [Cu(L2)Cl]·H_2O **2a** and [Cu(L2)NO_3]·H_2O **3a**) showed potential anticancer activity *in vitro* [22, 35], we synthesized the corresponding 1:1:1 Cu(II)/ligand/co-ligand complexes ([Cu(L1)(Py)Cl]·H_2O **1b**, [Cu(L2)(Py)Cl] **2b** and [Cu(L2)(Py)NO_3] **3b**) to assess their anticancer activity, where L1 and L2 are the tridentate (*E*)-*N'*-(2-hydroxybenzylidene)acetohydrazide ligand and (*E*)-*N*'-(2-hydroxybenzylidene)benzohydrazide ligand, respectively (Scheme 1). Even though there are a wide variety of mixed-ligand copper complexes that have been proposed as promising cytotoxic agents, only a few studies have attempted to investigate their working mechanisms [5]. Therefore, among the six complexes proposed, we chose the 1:1:1 Cu(II)/ligand/co-ligand complex **3b** to be further investigated for its anticancer mechanism.

2. Experimental section

2.1. Materials

All reagents and solvents for synthesis and analysis were commercially available. H_2O used in all reactions was distilled prior to use. Elemental (C, H and N) analyses were carried out on an Elementar Vario Micro Cube elemental analyzer. Infrared spectra (IR) were measured using KBr pellets (400−4000 cm^{-1}) on a Nexus 870 FT-IR spectrophotometer. The high resolution electrospray ionization-mass spectroscopy (HRMS-ESI) was recorded on Exactive liquid chromatography-MS mass spectrometer (Thermofisher Scientific, USA). UV-Vis spectra were recorded on a Cary 1E UV−Visible spectrophotometer. The fluorescence spectra were recorded on a MPF-4 spectrofluorometer.

2.2. Synthesis of copper(II) complexes

The ligands (*E*)-*N'*-(2-hydroxybenzylidene)acetohydrazide (L1), (*E*)-*N'*-(2-hydroxybenzylidene)benzohydrazide (L2), and complexes $[Cu(L1)Cl]\cdot 2H_2O$ (**1a**) $[Cu(L2)Cl]\cdot H_2O$ (**2a**) and $[Cu(L2)NO_3]\cdot H_2O$ (**3a**) were synthesized according to literature procedures (shown in Supplementary Material) [36-38].

Synthesis of complex $[Cu(L1)(Py)Cl]\cdot H_2O$ (1b). The complex was prepared by adding L1 solution in methanol (0.17 g, 1 mmol) and pyridine (0.08 g, 1 mmol) into $CuCl_2\cdot 2H_2O$ solution in methanol (0.17 g, 1 mmol). The reaction mixture was stirred for 1 h at ambient temperature to obtain a clear blue solution. Dark green block crystals for X-ray structural characterization were obtained by a slow evaporation process of the blue solution after five days. Yield: 61%. Anal. Calcd for $C_{14}H_{16}ClCuN_3O_3$ (373.29): C 45.05, H 4.32 and N 11.25; found: C 45.27, H 4.41 and N 11.55. IR (KBr, cm-1): 3357m, 3039w, 2731w, 1607vs, 1559vs, 1528s, 1497w, 1447m, 1385s, 1324m, 1251w, 1210m, 1149m, 1110w, 1080w, 1039w, 998w, 898w, 773m, 697m, 642w, 612w and 476w.

Synthesis of complexes [Cu(L2)(Py)Cl] (2b) and $[Cu(L2)(Py)NO_3]$ (3b). L2 (0.24 g, 1 mmol) and pyridine (0.08 g, 1 mmol) were dissolved in 15 mL of methanol. The mixture was stirred for 10 min to produce a yellow solution, which was then added to a methanol solution (10 mL) of the mixed copper(II) salts ($CuCl_2\cdot 2H_2O$: 0.17 g, 1 mmol for **2b**; $Cu(NO_3)_2\cdot 3H_2O$: 0.24 g, 1 mmol for **3b**). The reaction mixture was stirred for another 1 h at ambient temperature to obtain a clear blue solution. Dark green block crystals were obtained after five days by evaporating the blue solution slowly, which were then examined by X-ray diffraction spectroscopy.

Complex **2b** (Yield: 76.8%): Elemental analysis calcd (%) for $C_{19}H_{16}ClCuN_3O_2$: C 54.68, H 3.86 and N 10.07; found: C 54.85, H 3.72 and N 10.22. IR (KBr, cm^{-1}): 3457m, 2946m, 2785m, 1608vs, 1552vs, 1445s, 1388s, 1347m, 1312m, 1201m, 1146m, 1068w, 892w, 796w, 756m, 693vs, 581w, 539w, 497w and 441w.

Complex **3b** (Yield: 82.1%): Elemental analysis calcd (%) for $C_{19}H_{16}CuN_4O_5$: C51.41, H 3.63. and N, 12.61; found: C 51.52, H 3.72 and N 12.75. IR (KBr, cm^{-1}): 3038m, 1604vs, 1540w, 1499vs, 1444vs, 1379vs, 1348s, 1284m, 1197m, 1146m, 1067m, 1035m, 946w, 892m, 757m, 697vs, 634w, 587w, 552w, 500w and 453w.

2.3. Crystal structure determinations

The single crystal data collection of complexes **1b**-**3b** were carried out on a SuperNova CCD Area Detector equipped with graphite monochromated Mo-Ka (λ = 0.71073 Å) radiation at room temperature. SADABS program were applied for empirical adsorption corrections of all data. The structures of the Cu(II) complexes were solved by direct methods and refined by full-matrix least-squares methods (against F^2) using the SHELXTL-2014 [39]. All non-H atoms were refined anisotropically. The crystallographic data for complexes **1b**-**3b** are summarized in Table S1 and Table 1. Crystallographic data for the structural analyses have been deposited at the Cambridge Crystallographic Data Centre (CCDC), reference numbers 1587786 for **1b**, 1033106 for **2b** and 1011406 for **3b**.

2.4. Cell lines

The human lung carcinoma A549 cell lines, A549cisR (cisplatin-resistant cell lines), human hepatocellular Bel-7402 cell lines, human breast cancer line MCF-7 cell lines and normal lung fibroblast WI-38 cells were obtained from American Type Culture Collection (ATCC, Manassas, VA). These cells were cultured in DMEM (with $_{L}$−glutamin) culture media supplemented with 1% antibiotic-antimycotic solution and 10% fetal bovine serum (FBS) at 37 °C and 5% CO_2.

2.5. Cytotoxicity assay

The cytotoxicity of all the test compounds was examined by a previously reported method using an MTT (3-(4,5-dimethylthiazol-2-yl)-2,5-diphenyltetrazolium bromide) assay. In brief, 100 μL of the cell line was seeded into each well of 96-well plates at 5 × 10^4 cells/mL and allowed to adhere for 24 h at 37 °C under 5% CO_2. Thereafter, the test compounds in a concentration range of 0−50 μM were added to the plates and incubated for 48 h at 37 °C under 5% CO_2. A total of 10 μL MTT (5 mg/mL) saline solution was added into each well and then incubated for 5 h at 37 °C under 5% CO_2. The medium was then discarded, and 100 μL of DMSO (dimethyl sulfoxide) was added into each well. The absorbance of each well was recorded at 570 nm by using an enzyme-labeling instrument (SpectraMax M5, Molecular Devices).

2.6. Cell morphology analysis

The assay was performed with MCF-7 cells. The MCF-7 cells (1 × 10^5 cells/mL) were seeded in six-well plates for 24 h at 37 °C under 5% CO_2 and then incubated with Cu(II) complexes (2 μM) at 37 °C for another 24 h. Thereafter, the cells were visualized under a bright-field microscope.

2.7. Cellular uptake study

The intracellular uptake of Cu(II) complexes was performed with MCF-7 cells. Briefly, 2×10^6 cells were seeded in 10 cm culture dishes at 37 °C under 5% CO_2. After 24 h, the medium was replaced, and the cells were incubated with the copper(II) complexes (4 μM) for 6 h. The cells were then carefully washed with phosphate buffered saline (PBS) several times and harvested by trypsinization. Cell digestion was performed using 3 mL of HNO_3 for 2 h at 60 °C. The copper content in the cells was analyzed using a graphite furnace atomic absorption spectrometer (GF-AAS).

2.8. Anticancer mechanism of the 3b complex

2.8.1. DNA binding and cleavage studies

Electronic absorption spectra in the range of 200–700 nm were recorded by increasing the amounts of calf-thymus DNA (CT-DNA) introduced to the test complex (35 μM) in pH 7.2 buffer (5 mM Tris-HCl/50 mM NaCl) at room temperature. For each addition, the samples were allowed to equilibrate for 10 min, and any changes in the absorption spectra were recorded.

Emission spectra in the range of 530–750 nm were determined by setting the excitation wavelength to 510 nm. The test complex was added to a mixture containing 10 μM CT-DNA and 8 μM ethidium bromide (EB) in pH 7.2 Tris-HCl buffer. The apparent binding constant (K_{app}) of the **3b** complex was measured using the following equation [40]:

$$K_{EB}\,[EB] = K_{app}\,[\text{complex}] \quad (1)$$

where $K_{EB} = 1 \times 10^7\ M^{-1}$, and [complex] is the concentration of the **3b** complex, thus causing a one-half reduction of the fluorescence intensity of the EB-CT-DNA system.

Viscosity experiments were conducted using Micro Ubbelohde viscometer at 25 ± 0.5 °C. The concentration of CT-DNA was fixed at 200 μM, whereas **3b** and EB concentrations were varied from 0 to 100 μM in pH 7.2 Tris-HCl buffer. Data were presented as $(\eta/\eta_o)^{1/3}$ vs. [compound]/[DNA], where η and η_o represent the viscosity of the CT-DNA solution in the presence and absence of the test compounds, respectively.

The efficiency of the **3b** complex to cleave DNA was monitored using agarose gel electrophoresis. In this study, a total volume of 20 μL in each reaction mixture contained supercoiled plasmid pBR322 DNA (200 ng), Tris-HCl buffer pH 7.0, and different concentrations (25, 50, and 100 μM) of the **3b** complex. The mixtures were

then incubated at 37 °C. After 3 h, 4 μL of 5X loading buffer was added. Subsequently, the reaction mixtures were loaded into 1% agarose gel (1 mg/mL in TAE) containing 1% (v/v) GoldView II and then analyzed using gel electrophoresis in 1X TAE buffer at 100 V for 90 min.

2.8.2. Topoisomerase I inhibition assay

The human topoisomerase I (Topo I) inhibitory activity by the **3b** complex was studied in the agarose gel electrophoresis experiments. One unit of Topo I was incubated with 0.25 μg supercoiled pBR322 plasmid DNA in the presence of each test complex (0–25 μM) in a buffer containing the following: 35 mM Tris-HCl (pH 8.0), 72 mM KCl, 0.1% BSA, 5 mM DTT (dithiothreitol), 5 mM spermidine, and 5 mM $MgCl_2$. The final volume of each sample was 20 μL. The mixtures were then incubated at 37 °C for 30 min, and the reaction was stopped by adding a loading buffer solution (4.5% sodium dodecyl sulfate, 45% glycerol, and 0.25% bromophenol blue) into each mixture. Electrophoresis was performed in a 0.8% agarose gel in 1X TAE buffer at 70 V for 120 min.

2.8.3. Molecular docking studies

To obtain the binding information of the **3b** complex toward DNA and Topo I, docking studies were performed using Autodock Vina [41]. The crystal structures of the DNA ($d(CGCGAATTCGCG)_2$) and human Topo I were obtained from the protein data bank (PDB ID: 1BNA and 1T8I, respectively). AutoDock program tools were utilized to delete the water molecules, add polar hydrogen atoms, and assign other parameters. In the docking studies, the single bonds of the Cu(II) complex were allowed to rotate, but the human Topo I and DNA structures were set to remain rigid.

2.8.4. Cell apoptosis

For the apoptosis experiments, Annexin V FITC kit (Sigma Aldrich, Missouri, USA) was used. MCF-7 cells were seeded in six-well plates and then incubated with the **3b** complex at different concentrations (0–2 μM). After 24 h, the cells were harvested and then resuspended in 1X annexin binding buffer (200 μL). Subsequently, 5 μL annexin V and 5 μL propidium iodide (PI) were added to each sample, and the mixtures were incubated on ice in the dark. An additional amount of binding buffer (300 μL) was added after 20 min, and the cells were analyzed immediately by flow cytometry.

2.8.5. Change in mitochondrial membrane potential assay

The mitochondrial membrane potential was analyzed in the presence of JC-1 probe (Beyotime Jiangsu China). MCF-7 cells were exposed to the **3b** complex (0–2 μM) for 24 h at 37 °C. Subsequently, the cells were harvested and then resuspended in a prewarmed JC-1 solution (5 μg/mL in PBS). After incubating for 30 min at 37 °C in the dark, the samples were washed three times with PBS and immediately measured by flow cytometry.

2.8.6. Detection of intracellular reactive oxygen species

Intracellular reactive oxygen species (ROS) production was measured with 2',7'-dichlorofluorescein diacetate probe (DCFH-DA) (Beyotime Jiangsu China). MCF-7 cells were incubated with the **3b** complex (0–2 μM) for 24 h. The cells were then harvested and washed three times with PBS, followed by resuspension in 500 μL of a serum-free medium containing 10 μM DCFH-DA probe. After 30 min of incubation at 37 °C in the dark, the samples were rewashed three times and suspended in 1 mL of PBS. The ROS generation in the MCF-7 cells was immediately measured by flow cytometry.

2.8.7. Western blot analysis.

Immunoblotting analysis was carried out as previously described [26, 42]. Primary antibodies: mouse anti-β-actin (Abcam), rabbit anti-γH2AX (Abcam), rabbit anti-phos-CHK1 (Abcam), rabbit anti-phos-CHK2 (Abcam), rabbit anti-phos-p53 (Abcam), mouse anti-cleaved caspase-9 (Abcam), mouse anti-cytochrome c (Abcam), mouse anti-cleaved caspase-3 (Abcam) and mouse anticleaved PARP-1 (Abcam). Secondary antibodies: horseradish peroxidase-conjugated sheep anti-mouse and horseradish peroxidase-conjugated donkey anti-rabbit (Cell Signalling Technology).

2.9. Inhibition of tumor spheroid growth

Three-dimensional spheroids were prepared according to a previously reported method [43]. Briefly, 1.5% (wt/v) agarose DMEM solution was heated to 80 °C for 30 min and then autoclaved for 30 min. Subsequently, 50 μL of agarose solution was pipetted into each well of a 96-well microtiter plate under sterile condition. After the agarose solidified, the agarose-coated plates were stored at ambient temperature and covered until use. Each 20 μL drop of MCF-7 cell (5000 cells/drop) was prepared on the upper lip of a cell culture petri dish and incubated in an inverted position at 37 °C under 5% CO_2. After 72 h, one multicellular spheroid was transferred to each agarose-coated well, and 200 μL of DMEM media was added into each well.

Thereafter, MCF-7 spheroids were allowed to settle for 24 h in a humidified CO_2 incubator followed by incubation with the test Cu(II) complexes at various concentrations.

2.10. Statistical analysis

All biological experiments have been carried out at least thrice with triplicatesin each experiment. Student's *t* test was performed to evaluate the significance of the measurement differences. Results were expressed as mean ± SD (standard deviations) and considered to be significant when $p< 0.05$.

3. Results and discussion

3.1. Description of structures

The structure of **1b** together with the atom labels scheme is shown in Fig. 1A. In complex **1b**, the monoanionic ONO tridentate $L1^-$ ligand is coordinated to copper(II) through the azomethine nitrogen (N2), deprotonated phenolic oxygen (O2) and the ketoamide oxygen (O1) forming respectively six- and five-membered chelate rings. In **1b**, the fourth coordination site is occupied by the pyridine nitrogen atom (N3), and completing the coordination sphere in the apical site is a Cl^- anion. In **1b**, the coordination geometry around the Cu(II) could be described as distorted square pyramid as evident from the trigonality parameter [44], $\tau = (\beta - \alpha)/60 = 0.091$, where β and α are the N2−Cu1−N3 (171.6°) and O2−Cu1−O1 (166.1°) angles, respectively. In the crystal packing of **1b**, the discrete copper(II) units were linked into a 1D polymeric chain by the N1−H1···O3 hydrogen bonds and bifurcated O3−H3A···Cl1^{i} and O3−H3B···Cl1^{iii} interactions (Fig. 1B).

Views of the asymmetric unit of **2b** and **3b** with atom labels are shown in Fig. 1C. The asymmetric units contain one tridentate $L2^-$ ligand, one Cu(II) center, a coordinated pyridine molecule, and one Cl/NO_3^- anion. In **2b**, the copper atoms exhibits a five-coordinate environment with a nitrogen atom and two oxygen atoms from a Schiff base-ligand, a nitrogen atom from the pyridine ligand, and one terminal Cl atom (Fig. 1C). In **2b** the coordination polyhedron around the Cu1 center could be described as a slightly distorted square pyramid ($\tau = 0.0001$), with the metal displaced from the O1/N2/O2/N1 basal plane (maximum displacement 0.005 Å for the N2 atom), and the Cl atom at the apex, with the metal displaced by 0.22 Å toward Cl

from the mean basal plane. In **3b**, the coordination geometry around copper(II) in the complex is very similar to that in **2b**; the only difference is the presence of a NO_3^- anion at the apical position (Fig. 1E). In **3b** the index of the degree of trigonality, τ, has a value 0.004, indicating a much more distorted structure compared to **2b**. All Cu−X bond distances of **2b** and **3b** are in good agreement with those found in the **1b** complex (Table S1). In solid state of **2b**, the dimers are formed via N−H···Cl interactions involving a nitrogen atom (N3) from a Schiff-base ligand and a chloride atom ($Cl1^i$) bonded to the $Cu1^i$ from the adjacent molecule ($N3\cdots Cl1^i$ = 3.11 Å and the $N1-H1\cdots Cl1^i$ angle is 156.2°, symmetry code: (i) 1 − x, 1 − y, 1 − z, Fig. 1D). Furthermore, a small extent of π···π stacking (Fig. 1D) between pyridine rings is noted in **2b**, a fact that could provide some stability to the dimeric structure. In **3b**, the monomeric units are interlinked by the NO_3^- anions through the N−H···O hydrogen bonds (Fig. 1F), which leads to a dimer fashion, and then a self-assembly of dimers by means of π···π stacking affords a one-dimensional (1D) polymeric chain (Fig. 1G).

3.2. Mass spectrometry

In order to confirm the structures found in the solid state and the stability of the ligand/co-ligand of these complexes in solution, these Cu(II) complexes were dissolved in methanol containing 10% (v/v) DMSO and then characterized by electrospray ionization mass spectrometry (ESI-MS) (Fig. 2). When the in-source energy was 0 eV, the ESI-MS spectrum of the **1a** complex showed the parent signal at *m*/*z* = 239.99, which could be assigned as isotopic envelopes corresponding to $[(L)Cu(L1)]^+$ (fit: 240.00), thus suggesting that the solvent H_2O molecules and the coordinated Cl^- anion were lost under electrospray ionization conditions. The parent cluster ions of **2a** and **3a** complexes were both found at *m*/*z* = 334.04, which could correspond to the $[Cu(L2) + CH_3OH]^+$ structure (fit: 334.04), thus suggesting that the coordinated anions were replaced by CH_3OH (methanol). Furthermore, some lower *m*/*z* species were found at 380.03 and 302.01, which could be assigned as $[Cu(L2) + DMSO]^+$ (fit: 380.03) and $[Cu(L2)]^+$ (fit: 302.01), respectively.

In the ESI-MS spectrum of **1b**, the ion peak at *m*/*z* 319.04 was assignable to $[Cu(L1)(Py)]^+$ (fit: 319.04), which was formed by losing the coordinated Cl^- anion and the solvent H_2O molecules. The ESI-MS spectra of **2b** and **3b** displayed similar fragmentation patterns and showed molecular parent ion peaks at *m*/*z* = 381.05 for $[Cu(L2)(Py)]^+$ (fit: 381.05), thus suggesting that **2b** and **3b** have the same structures

in the solution. These results are in good agreement with the proposed structures. The results also indicated that the ligand/co-ligand of these Cu(II) complexes were essentially inert in the solution.

3.3. *In vitro* cytotoxicity

The *in vitro* anticancer activity of the **1a**–**3a** and **1b**–**3b** complexes, the free Schiff base ligands (L1 and L2), and the co-ligand was evaluated in a panel of human cancer cell lines by the MTT test. For comparison, the anticancer activity of *cis*platin was also examined under identical conditions.

Table 2 shows the IC_{50} values. All Cu(II) complexes showed micromolar toxicities (1.12–47.36 μM), which were comparable to and in many cases significantly better than that of *cis*platin. The IC_{50} values of the 1:1:1 Cu(II)/ligand/co-ligand complexes **1b**–**3b** were significantly lower ($p < 0.01-0.05$) than those of the corresponding 1:1 Cu(II)/ligand complexes **1a**–**3a**, thus indicating that the introduction of the co-ligand pyridine moiety into **1a**–**3a** enhanced the anticancer activity of **1a**–**3a**. The **1b** complex was 2.76-, 2.95-, 7.75-, and 7.74-fold more cytotoxic ($p < 0.01$) than the **1a** in Bel-7402, MCF-7, A549, and A549cisR cells, respectively. The IC_{50} values of **2b** were 1.91-, 3.12-, 1.40-, and 1.48-fold lower ($p < 0.05$) than those of **2a** in Bel-7402, MCF-7, A549, and A549cisR cells, respectively. Similarly, the IC_{50} values of **3b** in Bel-7402, MCF-7, A549, and A549cisR cells were 2.09-, 3.43-, 1.46-, and 1.47-fold lower ($p < 0.05$) (i.e., more cytotoxic) than those of **3a**, respectively. These results suggested that the introduction of pyridine co-ligand affected the type and number of ligands, as well as the coordination geometry in the complexes, thus leading to a change in the hydrophobicity of the Cu(II) complexes, an increase in cellular uptake (vide infra), and an improvement in the anticancer activity of the Cu(II) complexes.

As revealed by the observed mean of IC_{50} values, the potency of the **1a**–**3a** to kill cancer cells followed the order **3a** ≈ **2a** > **1a** and that of **1b**–**3b** followed the order **3b** ≈ **2b** > **1b**. None of the Cu(II) complexes displayed any cross-resistance with *cis*platin, as ascertained by their ability to kill the A549cisR and A549 cell lines indiscriminately. The co-ligand, the free Schiff base ligands, and the Cu(II) salts showed relatively low activity against cancer cells, thus implying that the anticancer activities by these Cu(II) complexes were derived from themselves altogether and not merely from the free Cu(II) chaperoned into the cancer cells by these ligands.

Furthermore, the cytotoxicities of these complexes were also evaluated in normal human WI-38 cells. In general, **2a**, **3a**, and **1b**–**3b** complexes were less potent toward WI-38, thus suggesting selective toxicity toward cancer cells over normal cells.

3.4. Cell morphology analysis

Fig. 3A depicts the effects of these Cu(II) complex (2 μM) treatments on the morphology of MCF-7 cells. The cells under treatment with **1a** and **1b** complexes exhibited similar cell morphologies (spindle shaped and anchorage dependent) to that of the control cells. However, the cells treated with other Cu(II) complexes, particularly **2b** or **3b**, were found to be mainly spherically shaped and lucent, thus indicating that the cell bodies were damaged. These results suggested that the apparent change in MCF-7 cell morphology was induced by the **2a**, **3a**, **2b**, and **3b** cytotoxic Cu(II) complexes.

3.5. Cellular uptake

Most previous studies reported that the cytotoxicity of metal complexes was correlated with their cellular uptake [45, 46]. Thus, the cellular uptake was investigated by treating MCF-7 cancer cells with 4 μM of **1a**–**3a** and **1b**–**3b** for 6 h. The intracellular Cu amount was then quantified by GF-AAS, and the results are shown in Fig. 3B. As expected, the results showed that the uptake of the **1b**, **2b**, and **3b** complexes were 1.51-, 1.57-, and 1.56- fold greater ($p < 0.05$) than that of the **1a**, **2a**, and **3a** complexes, respectively, thus corroborating their cytotoxicity results. It can be speculated that the internalization of these Cu(II) complexes might play a vital role in their cellular cytotoxicity.

3.6. Possible anticancer mechanism of the 3b complex

3.6.1. DNA binding and cleavage studies

Considering that **3b** or **2b** showed the most potent cytotoxic effects compared with the other analogs, the **3b** complex was selected for further investigation. DNA is the important intracellular anticancer target of many metallodrugs [5, 47, 48]. Therefore, metallodrug–DNA interactions are important for understanding the anticancer mechanisms of metal-based drugs.

To investigate the binding of the **3b** complex to CT-DNA, multiple spectroscopic techniques were used. In this study, the UV-Vis absorption spectra of **3b** in the presence and absence of CT-DNA were recorded (Fig. 4A). The observed peaks in the UV region are characteristics of $\pi-\pi^*$ for ligand transitions. Owing to the addition of

CT-DNA to the test complex, the absorption bands of the **3b** complex at 308 and 377 nm exhibited hypochromisms of approximately 14.1% and 8.4%, respectively, with a hypochromic shift of ca. 2 nm in the above band positions. The results indicated a strong interaction between the **3b** complex and CT-DNA, and it is possible that the **3b** complex bound to the CT-DNA helix via intercalation.

To further study the binding mode of the **3b** complex to CT-DNA, EB displacement studies were performed. As shown in Fig. 4B, the emission intensity decreased by approximately 63.8% with the addition of 25 μM of the **3b** complex to the EB-CT-DNA system, thus showing that the **3b** complex efficiently competed with EB and that the **3b** complex could interact with CT-DNA possibly by intercalative mode [49]. The binding constant (K_{app}) values were obtained for the **3b** complex by using Equation (1). The K_{app} value ($2.67 \pm 0.15 \times 10^6$ M^{-1}) of **3b** was less than the binding constant value (10^7 M^{-1}) of classical intercalators and metallointercalators, thus suggesting that the interaction between CT-DNA and the **3b** complex occurred via a moderate intercalative mode.

The viscosity of CT-DNA, which is sensitive to changes in DNA length, was measured to analyze the binding nature of the **3b** complex with CT-DNA. As depicted in Fig. 4C, the viscosity of CT-DNA increased with increasing **3b** complex concentration, thus proving that the binding of the **3b** complex to CT-DNA was via intercalation.

Docking studies were performed to provide conclusive results and complement the spectroscopic results into the insight of complex−DNA interaction. The B-DNA scaffold from 1BNA was used in a broad search for the complex–DNA interactions of the **3b** complex. Fig. 4D shows the energetically favorable docked poses obtained from the molecular docking of the **3b** complex with the B-DNA. The results showed that the Cu(II) complex fitted well into the curved contour of the B-DNA into the minor groove region situated within the A−T rich region. The energy minimized structure suggested that the Cu(II) complex was stabilized by hydrophobic contacts and van der Waals forces with the B-DNA functional groups. In this model, the L2 ligand of the **3b** complex was inside the minor groove, whereas the pyridine group (co-ligand) of the **3b** complex pointed outside of the minor groove. Moreover, the nitrogen atoms (N2 and N3) of the Cu(II) complex might be engaged by

hydrogen-bonding interactions with the DNA nucleobases DA-6 ($NH_{DA}\cdots N3$ = 3.13 Å) and DT-20 ($N2-H2\cdots O_{DT}$ = 2.54 Å).

The ability of the **3b** complex to cleave supercoiled pBR322 plasmid DNA was assessed by gel electrophoresis. Fig. 4E shows the results of the agarose gel electrophoretic separations of the supercoiled pBR322 plasmid DNA with increasing concentrations of the **3b** complex. The Cu(II) complex could relax the Form I (supercoiled form) of DNA into Form II (open circular form) in a dose-dependent manner. The aforementioned results collectively implied that the **3b** complex could interact with the DNA target and might lead to DNA damage in cancer cells.

3.6.2. Topoisomerase I inhibition

DNA Topo I is an essential nuclear enzyme and is vital for the topological change of DNA [50]. Topo I poisoning can disturb the topoisomerase in cancer cells by inducing DNA damage that ultimately leads to cell apoptosis [51]. Topo I is currently considered a significant intracellular target for anticancer drugs [5]. Therefore, the effects of the **3b** complex on the activity of human Topo I by agarose gel electrophoresis were investigated. The result showed that the Cu(II) complex significantly prevented the unwinding of DNA by the action of human Topo I at concentrations as low as 12.5 μM, thus indicating that the complex was the inhibitor of human Topo I (Fig. 4F).

Docking studies were further performed to explore the potential interaction mode of the **3b** complex with Topo I. As depicted in Fig. 4G, the phenyl group of the Cu(II) complex was intercalated onto the DNA cleavage site of Topo I and formed base-stacking interactions with both T10 (–1) and G11 (+1) base pairs. Furthermore, the O1 atom and N3 atom of the Cu(II) complex formed hydrogen-bonding interactions with Thr718 and Arg364, respectively. The pyridine group pointed outside of the major groove and formed a hydrophobic interaction with IIe535. These results suggested that the Cu(II) complex fitted well into the DNA cleavage site and might suppress the association of the Topo I enzyme with DNA, thereby influencing the Topo I inhibition activity or the ability to form a stable complex with DNA.

3.6.3. Biomarkers of DNA damage

The results of the DNA binding, DNA cleavage studies, and Topo I inhibition assay suggested that the **3b** complex was likely to induce DNA damage. To further investigate whether the **3b** complex could induce DNA damage in cancer cells,

western blotting analyses were used to examine the expression of the biomarkers related to the DNA damage pathway. Accordingly, MCF-7 cells were incubated with the **3b** complex for 24 h, and the untreated cells were used as controls. As shown in Fig. 4H, the phosphorylated forms of p53 (Ser15), CHK1, CHK2, and H2AX (γH2AX) expressions were upregulated by the **3b** complex compared with the untreated controls, thus indicating DNA damage in MCF-7 cancer cells [52–54].

3.6.4. Analysis of apoptosis

Many anticancer agents evidently exert their cytotoxic effects by activating apoptosis [55]; hence, we investigated the features related to these pathways. To evaluate cell apoptosis in the presence of the **3b** complex, FITC-Annexin V/PI dual staining was performed in MCF-7 cells. Flow cytometry analysis showed that the **3b** complex could efficiently induce concentration-dependent apoptosis in MCF-7 cells (Fig. 5A).

3.6.5. Induction of mitochondrial damage

Mitochondria damage is tightly linked to apoptosis pathways [56, 57]. Interestingly, recent studies provided evidence for the differences in the structure and function of mitochondria in cancer and normal cells, thus providing us the opportunities to target mitochondria when designing anticancer agents [42, 58]. To establish whether the **3b** complex–induced apoptosis was related to mitochondrial damage, we examined the influence of the complex on the mitochondrial membrane potential ($\Delta\psi_m$) of MCF-7 cells by using the lipophilic fluorescent probe JC-1 (5,5',6,6'-tetrachloro-1,1',3,3'-tetraethyl-benzimidazolyl-carbocyanine iodide) staining method. JC-1 staining indicated a loss of $\Delta\psi_m$, as evidenced by a few JC-1 aggregates (indicating hyperpolarized mitochondria and showing red fluorescence) and increased JC-1 monomers (indicating depolarized mitochondria and showing green fluorescence). As shown in Fig. 5B, treating MCF-7 cells with the **3b** complex caused the loss of $\Delta\psi_m$ in a dose-dependent fashion, thus illustrating the activation of mitochondrial-mediated apoptosis pathway.

Another confirmation that the **3b** complex exerted apoptosis via the mitochondrial pathway was obtained from the western blotting analyses, which were conducted to monitor the expression levels of cytochrome c, cleaved caspase-3, cleaved caspase-9, and cleaved PARP-1 (poly ADP ribose polymerase 1). The cytochrome c in the mitochondria fraction was downregulated, whereas its amount in the cytoplasm was

upregulated (Fig. 5C), thus confirming that the treatment with the **3b** complex resulted in the loss of $\Delta\psi_m$ and the mitochondrial release of cytochrome c. As a result, the levels of cleaved caspase-3 and cleaved caspase-9 were upregulated. Subsequently, cleaved PARP-1 was also upregulated, thus regulating the apoptosis program of MCF-7 cells.

3.6.6. Elevation of ROS levels

Cell apoptosis induced by metal-based complexes is closely related to ROS generation [59]. Increased ROS can damage intracellular macromolecules and induce apoptosis or alter cell function [60–62]. Thus, we monitored how the treatment of MCF-7 cells with the **3b** complex could affect the production of intracellular ROS by using a fluorescent H_2DCFDA probe (2',7'-dichlorofluorescein diacetate). As shown in Fig. 5D, the cells treated with the **3b** complex had a right-shifted fluorescence peak relative to the control cells, thus confirming that the **3b** complex indeed induced ROS production. At a concentration of 1 μM, the **3b** complex increased the intracellular ROS level by ca. 40% compared to the control group (Fig. S1).

3.7. Inhibition of tumor spheroid growth

Multicellular tumor spheroids are superior to monolayer tumor cells in simulating internal solid tumor tissue because multicellular tumor spheroids mimic the tight cell–cell interactions, intricate cellular heterogeneity, and tumor microenvironment observed in vivo more closely [63, 64]. Therefore, multicellular 3D MCF-7 tumor spheroids were used in the current study to evaluate the potential of the **3b** complex to prevent the growth of solid tumors.

The inhibition of MCF-7 tumor spheroid growth was investigated after the treatment with the **3a** or **3b** complex at a concentration of 4 μM for seven days. As shown in Fig. 6, the MCF-7 tumor spheroids kept increasing in volume in the absence of Cu(II) complexes. The obvious volume reduction of the MCF-7 tumor spheroids was observed for the **3a** complex after a seven-day treatment, but the obtained 3D spheroids were compact. However, the tumor cells on the surface of MCF-7 tumor spheroids treated with the **3b** complex were more disorganized. Moreover, the cell membrane ruptured and the cell leaked. These results confirmed that the **3b** complex was more effective than the **3a** complex as an antitumor agent.

4. Conclusions

We presented a Cu-based platform for a possible anticancer agent by introducing a pyridine co-ligand into 1:1 Cu(II)/ligand complexes to form 1:1:1 Cu(II)/ligand/co-ligand complexes with a minor synthetic effort; this platform resulted in changes in biochemical properties. We demonstrated that the 1:1:1 Cu(II)/ligand/co-ligand complexes exhibited excellent *in vitro* anticancer activity and showed two- to eightfold better activity than the corresponding 1:1 Cu(II)/ligand complexes in Bel-7402, MCF-7, A549, and A549cisR cancer cell lines. Further mechanistic studies provided that the **3b** complex induces the DNA damage, resulting in an ROS-mediated mitochondrial dysfunction apoptosis pathway. In conclusion, the results of our study might potentially represent a powerful strategy for enhancing the anticancer activity of metal-based agents.

Acknowledgements

This work is supported by the Natural Science Foundation of Guangxi (2017GXNSFEA198002), High-level innovation team and distinguished scholar program of Guangxi universities to F. Yang, the National Natural Science Foundation of China (grant No.81503161) and the Technology Division of Nantong (MS12016022).

References

[1] Y. Jung, S.J. Lippard, Direct cellular responses to platinum-induced DNA damage, Chem. Rev., 107 (2007) 1387-1407.

[2] M.A. Fuertes, C. Alonso, J.M. Perez, Biochemical modulation of Cisplatin mechanisms of action: enhancement of antitumor activity and circumvention of drug resistance, Chem. Rev., 103 (2003) 645-662.

[3] P.C.A. Bruijnincx, P.J. Sadler, New trends for metal complexes with anticancer activity, Curr. Opin. Chem. Biol., 12 (2008) 197-206.

[4] C. Stefani, Z. Al-Eisawi, P.J. Jansson, D.S. Kalinowski, D.R. Richardson, Identification of differential anti-neoplastic activity of copper bis(thiosemicarbazones) that is mediated by intracellular reactive oxygen species generation and lysosomal membrane permeabilization, J. Inorg. Biochem., 152 (2015) 20-37.

[5] C. Santini, M. Pellei, V. Gandin, M. Porchia, F. Tisato, C. Marzano, Advances in copper complexes as anticancer agents, Chem. Rev., 114 (2014) 815-862.

[6] S.B. Chanu, S. Banerjee, M. Roy, Potent anticancer activity of photo-activated oxo-bridged diiron(III) complexes, Eur. J. Med. Chem., 125 (2017) 816-824.

[7] L. Ruiz-Azuara, M.E. Bravo-Gomez, Copper compounds in cancer chemotherapy, Curr. Med. Chem., 17 (2010) 3606-3615.

[8] B. Hassouneh, M. Islam, T. Nagel, Q. Pan, S.D. Merajver, T.N. Teknos, Tetrathiomolybdate promotes tumor necrosis and prevents distant metastases by suppressing angiogenesis in head and neck cancer, Mol. Cancer Ther., 6 (2007) 1039-1045.

[9] M.M. Eatock, A. Schatzlein, S.B. Kaye, Tumour vasculature as a target for anticancer therapy, Cancer Treat. Rev., 26 (2000) 191-204.

[10] H. Xie, Y.J. Kang, Role of copper in angiogenesis and its medicinal implications, Curr. Med. Chem., 16 (2009) 1304-1314.

[11] A. Gupte, R.J. Mumper, Elevated copper and oxidative stress in cancer cells as a target for cancer treatment, Cancer Treat. Rev., 35 (2009) 32-46.

[12] F. Tisato, C. Marzano, M. Porchia, M. Pellei, C. Santini, Copper in diseases and treatments, and copper-based anticancer strategies, Med. Res. Rev., 30 (2010) 708-749.

[13] T.B. Chaston, R.N. Watts, J. Yuan, D.R. Richardson, Potent antitumor activity of novel iron chelators derived from di-2-pyridylketone isonicotinoyl hydrazone involves fenton-derived free radical generation, Clin. Cancer Res., 10 (2004) 7365-7374.

[14] X. Bao, Y. Xue, C. Xia, Y. Lu, N. Yang, Y. Zhao, Synthesis and Assessment of Novel Anti-chlamydial Benzylidene Acylhydrazides Derivatives, Lett. Drug Des. Discov., 15 (2018) 31-36.

[15] K. Hrušková, E. Potůčková, T. Hergeselová, L. Liptáková, P. Hašková, P. Mingas, P. Kovaříková, T. Šimůnek, K. Vávrová, Aroylhydrazone iron chelators: Tuning antioxidant and antiproliferative properties by hydrazide modifications, Eur. J. Med. Chem., 120 (2016) 97-110.

[16] B. Samanta, J. Chakraborty, S. Shit, S.R. Batten, P. Jensen, J.D. Masuda, S. Mitra, Synthesis, characterisation and crystal structures of a few coordination complexes of nickel(II), cobalt(III) and zinc(II) with

N′-[(2-pyridyl)methylene]salicyloylhydrazone Schiff base, Inorg. Chim. Acta, 360 (2007) 2471-2484.

[17] G.M. Abu El-Reash, O.A. El-Gammal, A.H. Radwan, Molecular structure and biological studies on Cr(III), Mn(II) and Fe(III) complexes of heterocyclic carbohydrazone ligand, Spectrochim. Acta A Mol. Biomol. Spectrosc., 121 (2014) 259-267.

[18] N.H. Al-Shaalan, Synthesis, characterization and biological activities of Cu(II), Co(II), Mn(II), Fe(II), and UO2(VI) complexes with a new Schiff Base hydrazone: O-hydroxyacetophenone-7-chloro-4-quinoline hydrazone, Molecules, 16 (2011) 8629-8645.

[19] G.S.S. Firmino, M.V.N. de Souza, C. Pessoa, M.C.S. Lourenco, J.A.L.C. Resende, J.A. Lessa, Synthesis and evaluation of copper(II) complexes with isoniazid-derived hydrazones as anticancer and antitubercular agents, Biometals, 29 (2016) 953-963.

[20] D. Senthil Raja, E. Ramachandran, N.S.P. Bhuvanesh, K. Natarajan, Synthesis, structure and in vitro pharmacological evaluation of a novel 2-oxo-1,2-dihydroquinoline-3-carbaldehyde (2′-methylbenzoyl) hydrazone bridged copper(II) coordination polymer, Eur. J. Med. Chem., 64 (2013) 148-159.

[21] C. Fan, H. Su, J. Zhao, B. Zhao, S. Zhang, J. Miao, A novel copper complex of salicylaldehyde pyrazole hydrazone induces apoptosis through up-regulating integrin β4 in H322 lung carcinoma cells, Eur. J. Med. Chem., 45 (2010) 1438-1446.

[22] Y. Gou, Y. Zhang, J. Qi, Z. Zhou, F. Yang, H. Liang, Enhancing the copper(II) complexes cytotoxicity to cancer cells through bound to human serum albumin, J. Inorg. Biochem., 144 (2015) 47-55.

[23] Y. Gou, Y. Zhang, Z. Zhang, J. Wang, Z. Zhou, H. Liang, F. Yang, Design of an Anticancer Copper(II) Prodrug Based on the Lys199 Residue of the Active Targeting Human Serum Albumin Nanoparticle Carrier, Mol. Pharm., 14 (2017) 1861-1873.

[24] W.J. Lian, X.T. Wang, C.Z. Xie, H. Tian, X.Q. Song, H.T. Pan, X. Qiao, J.Y. Xu, Mixed-ligand copper(ii) Schiff base complexes: the role of the co-ligand in DNA binding, DNA cleavage, protein binding and cytotoxicity, Dalton Trans., 45 (2016) 9073-9087.

[25] N.P. Barry, P.J. Sadler, Exploration of the medical periodic table: towards new targets, Chem. Commun., 49 (2013) 5106-5131.

[26] Y. Gou, J. Li, B. Fan, B. Xu, M. Zhou, F. Yang, Structure and biological properties of mixed-ligand Cu(II) Schiff base complexes as potential anticancer agents, Eur. J. Med. Chem., 134 (2017) 207-217.

[27] V. Gandin, M. Porchia, F. Tisato, A. Zanella, E. Severin, A. Dolmella, C. Marzano, Novel mixed-ligand copper(I) complexes: role of diimine ligands on cytotoxicity and genotoxicity, J. Med. Chem., 56 (2013) 7416-7430.

[28] C. Rajarajeswari, M. Ganeshpandian, M. Palaniandavar, A. Riyasdeen, M.A. Akbarsha, Mixed ligand copper(II) complexes of 1,10-phenanthroline with tridentate phenolate/pyridyl/(benz)imidazolyl Schiff base ligands: covalent vs non-covalent DNA binding, DNA cleavage and cytotoxicity, J. Inorg. Biochem., 140 (2014) 255-268.

[29] D.A. Safin, M.P. Mitoraj, K. Robeyns, Y. Filinchuk, C.M. Vande Velde, Luminescent mononuclear mixed ligand complexes of copper(I) with 5-phenyl-2,2'-bipyridine and triphenylphosphine, Dalton Trans., 44 (2015) 16824-16832.

[30] X.Y. Qin, Y.N. Wang, X.P. Yang, J.J. Liang, J.L. Liu, Z.H. Luo, Synthesis, characterization, and anticancer activity of two mixed ligand copper(ii) complexes by regulating the VEGF/VEGFR2 signaling pathway, Dalton Trans., 46 (2017) 16446-16454.

[31] M. Sutradhar, Rajeshwari, T. Roy Barman, A.R. Fernandes, F. Paradinha, C. Roma-Rodrigues, M.F.C. Guedes da Silva, A.J.L. Pombeiro, Mixed ligand aroylhydrazone and N-donor heterocyclic Lewis base Cu(II) complexes as potential antiproliferative agents, J. Inorg. Biochem., 175 (2017) 267-275.

[32] R. Loganathan, M. Ganeshpandian, N.S.P. Bhuvanesh, M. Palaniandavar, A. Muruganantham, S.K. Ghosh, A. Riyasdeen, M.A. Akbarsha, DNA and protein binding, double-strand DNA cleavage and cytotoxicity of mixed ligand copper(II) complexes of the antibacterial drug nalidixic acid, J. Inorg. Biochem., 174 (2017) 1-13.

[33] B. Annaraj, C. Balakrishnan, M.A. Neelakantan, Synthesis, structure information, DNA/BSA binding affinity and in vitro cytotoxic studies of mixed ligand copper(II) complexes containing a phenylalanine derivative and diimine co-ligands, J. Photochem. Photobiol. B, 160 (2016) 278-291.

[34] M. Kumar, M. Srivastava, R.A. Yadav, Vibrational studies of benzene, pyridine, pyridine-N-oxide and their cations, Spectrochim. Acta. A Mol. Biomol. Spectrosc., 111 (2013) 242-251.

[35] E.W. Ainscough, A.M. Brodie, W.A. Denny, G.J. Finlay, S.A. Gothe, J.D. Ranford, Cytotoxicity of salicylaldehyde benzoylhydrazone analogs and their transition metal complexes: quantitative structure-activity relationships, J. Inorg. Biochem., 77 (1999) 125-133.

[36] M.F. Iskander, T.E. Khalil, R. Werner, W. Haase, I. Svoboda, H. Fuess, Synthesis, reactivity and magnetochemical studies on copper(II) complexes derived from N-salicylidenearoylhydrazines. X-ray structure of [mononitratoOO(−1)(N-salicylidenatobenzoylhydrazine)ONO(−1)]copper(II) monohydrate, Polyhedron, 19 (2000) 949-958.

[37] F.B. Tamboura, M. Gaye, A.S. Sall, A.H. Barry, Y. Bah, Chlorido[N'-(2-oxidobenzil-idene)acetohydrazide-κO,N',O']copper(II) dihydrate, in: Acta Crystallogr Sect E Struct Rep Online, 65 (2009) m160-161.

[38] A.A. Aruffo, T.B. Murphy, D.K. Johnson, N.J. Rose, V. Schomaker, Structural studies of Fe(III) and Cu(II) complexes of salycylaldehyde benzoyl hydrazone, a synthetic chelating agent exhibiting diverse biological properties, Inorg. Chim. Acta, 67 (1982) L25-L27.

[39] G.M. Sheldrick, *SHELXL2014/7*, University of Göttingen, Germany, 2014.

[40] M. Lee, A.L. Rhodes, M.D. Wyatt, S. Forrow, J.A. Hartley, GC base sequence recognition by oligoimidazolecarboxamide and C-terminus-modified analogs of distamycin deduced from circular dichroism, proton nuclear magnetic resonance, and methidiumpropylethylenediaminetetraacetate-iron(II) footprinting studies, Biochemistry, 32 (1993) 4237-4245.

[41] O. Trott, A.J. Olson, AutoDock Vina: improving the speed and accuracy of docking with a new scoring function, efficient optimization, and multithreading, J. Comput. Chem., 31 (2010) 455-461.

[42] Y. Ye, T. Zhang, H. Yuan, D. Li, H. Lou, P. Fan, Mitochondria-Targeted Lupane Triterpenoid Derivatives and Their Selective Apoptosis-Inducing Anticancer Mechanisms, J. Med. Chem., 60 (2017) 6353-6363.

[43] M. Asif, M.A. Iqbal, M.A. Hussein, C.E. Oon, R.A. Haque, M.B. Khadeer Ahamed, A.S. Abdul Majid, A.M.S. Abdul Majid, Human colon cancer targeted

pro-apoptotic, anti-metastatic and cytostatic effects of binuclear Silver(I)-N-Heterocyclic carbene (NHC) complexes, Eur. J. Med. Chem., 108 (2016) 177-187.

[44] A. Pal, B. Biswas, S.K. Mondal, C.-H. Lin, R. Ghosh, Copper(II) complexes with neutral Schiff bases: Syntheses, crystal structures and DNA interactions, Polyhedron, 31 (2012) 671-675.

[45] Y.R. Zheng, K. Suntharalingam, T.C. Johnstone, H. Yoo, W. Lin, J.G. Brooks, S.J. Lippard, Pt(IV) prodrugs designed to bind non-covalently to human serum albumin for drug delivery, J. Am. Chem. Soc., 136 (2014) 8790-8798.

[46] P. Nagababu, A.K. Barui, B. Thulasiram, C.S. Devi, S. Satyanarayana, C.R. Patra, B. Sreedhar, Antiangiogenic activity of mononuclear copper(II) polypyridyl complexes for the treatment of cancers, J. Med. Chem., 58 (2015) 5226-5241.

[47] A.D. Richards, A. Rodger, Synthetic metallomolecules as agents for the control of DNA structure, Chem. Soc. Rev., 36 (2007) 471-483.

[48] J. Wang, Y. Gou, Z. Zhang, P. Yu, J. Qi, Q. Qin, H. Sun, X. Wu, H. Liang, F. Yang, Developing an Anticancer Copper(II) Multitarget Pro-Drug Based on the His146 Residue in the IB Subdomain of Modified Human Serum Albumin, Mol. Pharm., 15 (2018) 2180-2193.

[49] M. Alagesan, N.S. Bhuvanesh, N. Dharmaraj, Binuclear copper complexes: synthesis, X-ray structure and interaction study with nucleotide/protein by in vitro biochemical and electrochemical analysis, Eur. J. Med. Chem., 78 (2014) 281-293.

[50] S.M. Cuya, M.-A. Bjornsti, R.C.A.M. van Waardenburg, DNA topoisomerase-targeting chemotherapeutics: what's new?, Cancer Chemother. Pharmacol., 80 (2017) 1-14.

[51] B. Montaner, W. Castillo-Avila, M. Martinell, R. Ollinger, J. Aymami, E. Giralt, R. Perez-Tomas, DNA interaction and dual topoisomerase I and II inhibition properties of the anti-tumor drug prodigiosin, Toxicol. Sci., 85 (2005) 870-879.

[52] K. Suntharalingam, T.C. Johnstone, P.M. Bruno, W. Lin, M.T. Hemann, S.J. Lippard, Bidentate ligands on osmium(VI) nitrido complexes control intracellular targeting and cell death pathways, J. Am. Chem. Soc., 135 (2013) 14060-14063.

[53] Y.-b. Guan, D.-r. Yang, S.-j. Nong, J. Ni, C.-h. Hu, J. Li, J. Zhu, Y.-x. Shan, Breviscapine (BVP) inhibits prostate cancer progression through damaging DNA by

minichromosome maintenance protein-7 (MCM-7) modulation, Biomed. Pharmacother., 93 (2017) 103-116.

[54] S. Burma, B.P. Chen, M. Murphy, A. Kurimasa, D.J. Chen, ATM phosphorylates histone H2AX in response to DNA double-strand breaks, J. Biol. Chem., 276 (2001) 42462-42467.

[55] P. Huang, D. Wang, Y. Su, W. Huang, Y. Zhou, D. Cui, X. Zhu, D. Yan, Combination of small molecule prodrug and nanodrug delivery: amphiphilic drug-drug conjugate for cancer therapy, J. Am. Chem. Soc., 136 (2014) 11748-11756.

[56] C. Wang, R.J. Youle, The Role of Mitochondria in Apoptosis, Annu. Rev. Genet., 43 (2009) 95-118.

[57] C. Wan, X. Ma, S. Shi, J. Zhao, X. Nie, J. Han, J. Xiao, X. Wang, S. Jiang, J. Jiang, Pivotal roles of p53 transcription-dependent and -independent pathways in manganese-induced mitochondrial dysfunction and neuronal apoptosis, Toxicol. Appl. Pharmacol., 281 (2014) 294-302.

[58] G.G. D'Souza, M.A. Wagle, V. Saxena, A. Shah, Approaches for targeting mitochondria in cancer therapy, Biochim. Biophys. Acta, 1807 (2011) 689-696.

[59] D. Trachootham, J. Alexandre, P. Huang, Targeting cancer cells by ROS-mediated mechanisms: a radical therapeutic approach?, Nat. Rev. Drug Discovery, 8 (2009) 579-591.

[60] Y. Lu, R. Zhang, S. Liu, Y. Zhao, J. Gao, L. Zhu, ZT-25, a new vacuolar H+-ATPase inhibitor, induces apoptosis and protective autophagy through ROS generation in HepG2 cells, Eur. J. Pharmacol., 771 (2016) 130-138.

[61] G.B. Jiang, X. Zheng, J.H. Yao, B.J. Han, W. Li, J. Wang, H.L. Huang, Y.J. Liu, Ruthenium(II) polypyridyl complexes induce BEL-7402 cell apoptosis by ROS-mediated mitochondrial pathway, J. Inorg. Biochem., 141 (2014) 170-179.

[62] J. Ge, C. Wang, X. Nie, J. Yang, H. Lu, X. Song, K. Su, T. Li, J. Han, Y. Zhang, J. Mao, Y. Gu, J. Zhao, S. Jiang, Q. Wu, ROS-mediated apoptosis of HAPI microglia through p53 signaling following PFOS exposure, Environ. Toxicol. Pharmacol., 46 (2016) 9-16.

[63] K.M. McMahon, M. Volpato, H.Y. Chi, P. Musiwaro, K. Poterlowicz, Y. Peng, A.J. Scally, L.H. Patterson, R.M. Phillips, C.W. Sutton, Characterization of changes in the proteome in different regions of 3D multicell tumor spheroids, J. Proteome Res., 11 (2012) 2863-2875.

[64] L. Lv, Y. Jiang, X. Liu, B. Wang, W. Lv, Y. Zhao, H. Shi, Q. Hu, H. Xin, Q. Xu, Z. Gu, Enhanced Antiglioblastoma Efficacy of Neovasculature and Glioma Cells Dual Targeted Nanoparticles, Mol. Pharm., 13 (2016) 3506-3517.

Figure captions

Scheme 1. Synthesis of the 1:1 Cu(II)/ligand complexes (**1a**-**3a**) and the 1:1:1 Cu(II)/ligand/co-ligand complexes (**1b**-**3b**).

Figure 1. (A) The local coordination environment of **1b**, H atoms are omitted for clarity. (B) Hydrogen bonding interactions (black dashed lines) of the **1b** complex with the surrounding moieties (Symmetry code: i = – *x*, – *y*, 1 – *z*; ii = 1 – *x*, – *y*, 1 – *z*; iii = 1 + *x*, *y*, *z*). (C) The local coordination environment of **2b**, H atoms are omitted for clarity. (D) Perspective view of a dimeric structure formed by hydrogen bonds (black dashed lines) and π··π stacking (blue dashed lines) in **2b** (Symmetry code: i = 1 – *x*, 1 – *y*, 1 – *z*). (E) The local coordination environment of **3b**, H atoms are omitted for clarity. (F) Perspective view of a dimeric structure formed by hydrogen bonds (black dashed lines) in **3b** (Symmetry code: i = 1 – *x*, – *y*, 2 – *z*). (G) Perspective view of a 1D chain formed by π··π stacking (blue dashed lines) and hydrogen bonds (black dashed lines) in **3b**.

Figure 2. ESI-MS spectra of **1a**-**3a** and **1b**-**3b** in MeOH containing DMSO (10% v/v) when the in-source energy was 0 eV. The red line simulated *m*/*z* envelope and black line is observed spectra.

Figure 3. (A) Change in morphology of MCF-7 cells in the presence of **1a**-**3a** and **1b**-**3b** (2.0 μM and 24 h). Scale bar: 500 μm. (B) MCF-7 cell uptake of **1a**-**3a** and **1b**-**3b** (*$p < 0.05$).

Figure 4. (A) Absorption spectra of the **3b** complex (35 μM) upon the titration of CT-DNA (0−32 μM). (B) Effect of addition of the **3b** complex on the emission intensity of EB (8 μM) bound to CT-DNA (10 μM) in a pH 7.2 Tris-HCl buffer. (C) Effect of increasing amounts of the **3b** complex or EB on the relative viscosity of CT-DNA (200 μM). (D) Molecular docked model of the **3b** complex with B-DNA (PDB ID: 1BNA). (E) Agarose gel electrophoresis patterns for the cleavage of pBR322 plasmid DNA by the **3b** complex at pH 7.2 at 37 °C for 5 h. Lane 1: DNA alone (control); Lanes 2−4: DNA with the **3b** complex at the concentrations of 25, 50, 100 μM, respectively. (F) Effect of the **3b** complex on Topo I mediated DNA relaxation; lane 1, DNA control; lane 2, Topo I + DNA; Lanes 3 and 4: DNA + Topo I with the **3b** complex at the concentrations of 12.5 and 25 μM, respectively. (G) Molecular docked model of the **3b** complex with the human-DNA Topo I (PDB ID:

1T8I). (H) Western blot analysis of proteins related to the DNA damage pathway in MCF-7 cells.

Figure 5. (A) Apoptotic effects of the **3b** complex on MCF-7 cells. MCF-7 cells were treated with the **3b** complex at the indicated concentrations for 24 h and then analyzed by flow cytometry after annexin V-FITC/PI staining. (B) Effects of the **3b** complex on mitochondrial membrane potential ($\Delta\psi_m$) analyzed by flow cytometry and JC-1 staining. (C) Effects of the **3b** complex on cytochrome c (in the cytoplasm and mitochondria, respectively), cleaved caspase-9, cleaved caspase-3, and cleaved PARP-1. MCF-7 cells were treated with the **3b** complex at the indicated concentrations for 24 h and then analyzed by Western blotting. (D) Analysis of ROS production by flow cytometry after MCF-7 cells was treated with vehicle or the **3b** complex for 24 h.

Figure 6. Morphology of 3D MCF-7 tumor spheroids treated with vehicle, **3a** or **3b** on at the indicated concentrations for 7 days. Scale bar: 200 μm.

Table 1 Crystal data for complexes **1b**-**3b**.

complex	**1b**	**2b**	**3b**
Empirical formula	$C_{14}H_{16}ClCuN_3O_3$	$C_{19}H_{16}ClCuN_3O_2$	$C_{19}H_{16}CuN_4O_5$
Molecular weight	373.29	417.34	443.91
Crystal system	triclinic	monoclinic	triclinic
Space group	$P-1$	$P2_1/c$	$P-1$
a/Å	8.8844(11)	7.627(4)	8.4027(6)
b/Å	9.6621(11)	20.335(11)	11.1825(11)
c/Å	9.8950(11)	11.502(6)	11.5411(9)
α/°	83.903(6)	90.00	62.413(9)
β/°	68.477(5)	95.388(9)	88.709(6)
γ/°	88.055(6)	90.00	79.905(7)
Volume/Å^3	785.70(15)	1775.9(17)	944.13(14)
Z	2	4	2
ρ_{calc}g/cm^3	1.578	1.561	1.561
μ(Mo−K$_\alpha$) (mm^{-1})	1.574	1.399	1.197
F(000)	382	852.0	454.0
Data/restraints/parameters	3589/0/203	3623/0/235	3857/0/262
Goodness−of−fit on F^2	1.093	1.054	1.056
Final R_1, wR_2 [$I > 2\sigma(I)$]	0.0476, 0.1113	0.0496, 0.1443	0.0505, 0.1405

Table 2 IC_{50} (μM) values of copper(II) complexes against panel of human cancer cell lines.

compound	cell growth inhibition, IC_{50} ± SD (μM)				
	Bel-7402	MCF-7	A549	A549cisR	WI−38
L1	> 50	> 50	> 50	> 50	> 50
L2	> 50	> 50	> 50	> 50	> 50
Py	> 50	> 50	> 50	> 50	> 50
Cu^{2+}	> 50	> 50	> 50	> 50	> 50
1a	16.22 ± 1.97	18.61 ± 2.18	47.36 ± 3.81	46.72 ± 5.33	18.36 ± 1.96
2a	4.42 ± 0.42	3.66 ± 0.38	5.27 ± 0.45	5.73 ± 0.62	9.94 ± 1.22
3a	4.76 ± 0.53	3.85 ± 0.33	5.36 ± 0.48	5.57 ± 0.34	9.83 ± 1.05
1b	5.86 ± 0.68	6.31 ± 0.72	6.11 ± 0.74	6.03 ± 0.51	9.16 ± 1.13
2b	2.31 ± 0.27	1.17 ± 0.15	3.74 ± 0.41	3.85 ± 0.39	5.67 ± 0.70
3b	2.27 ± 0.21	1.12 ± 0.23	3.65 ± 0.47	3.77 ± 0.34	5.59 ± 0.53
*Cis*platin	13.71 ± 1.35	21.25 ± 2.37	20.34 ± 1.97	> 50	19.67 ± 1.81

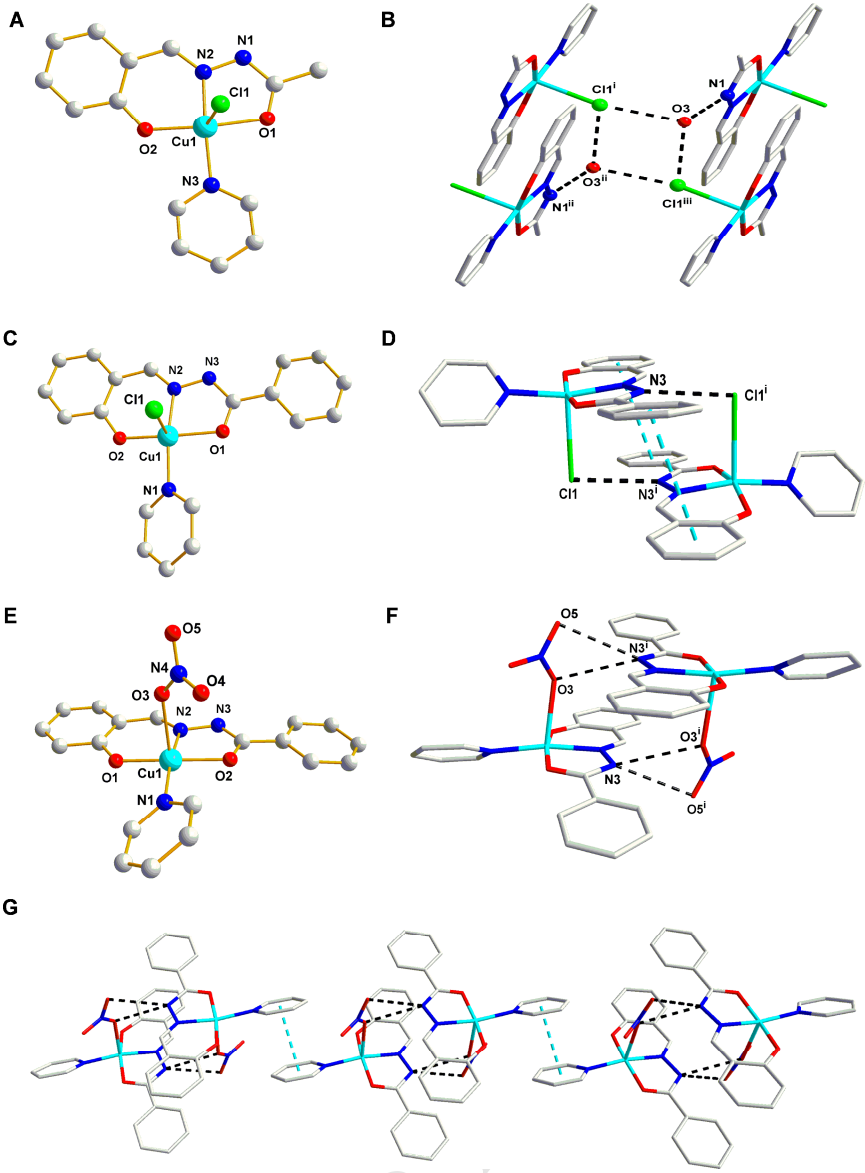

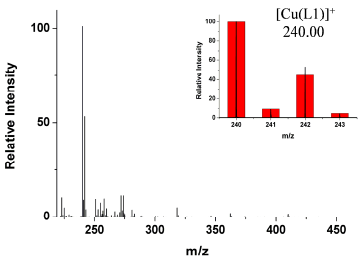

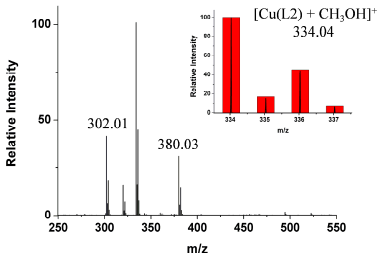

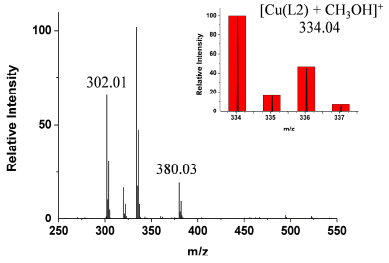

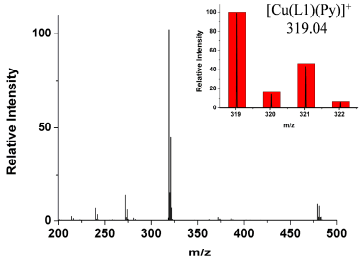

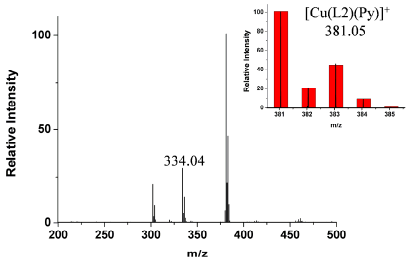

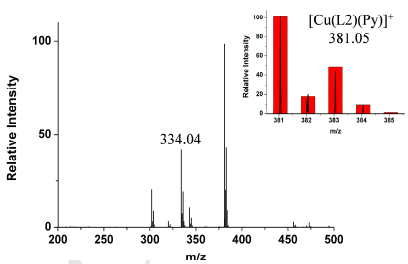

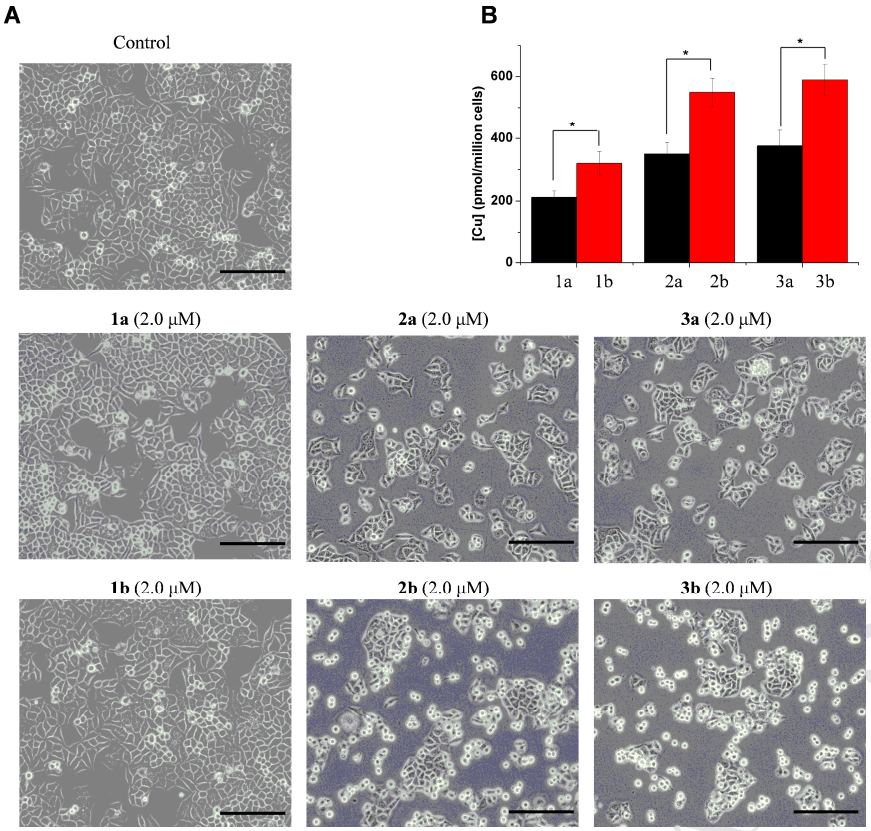

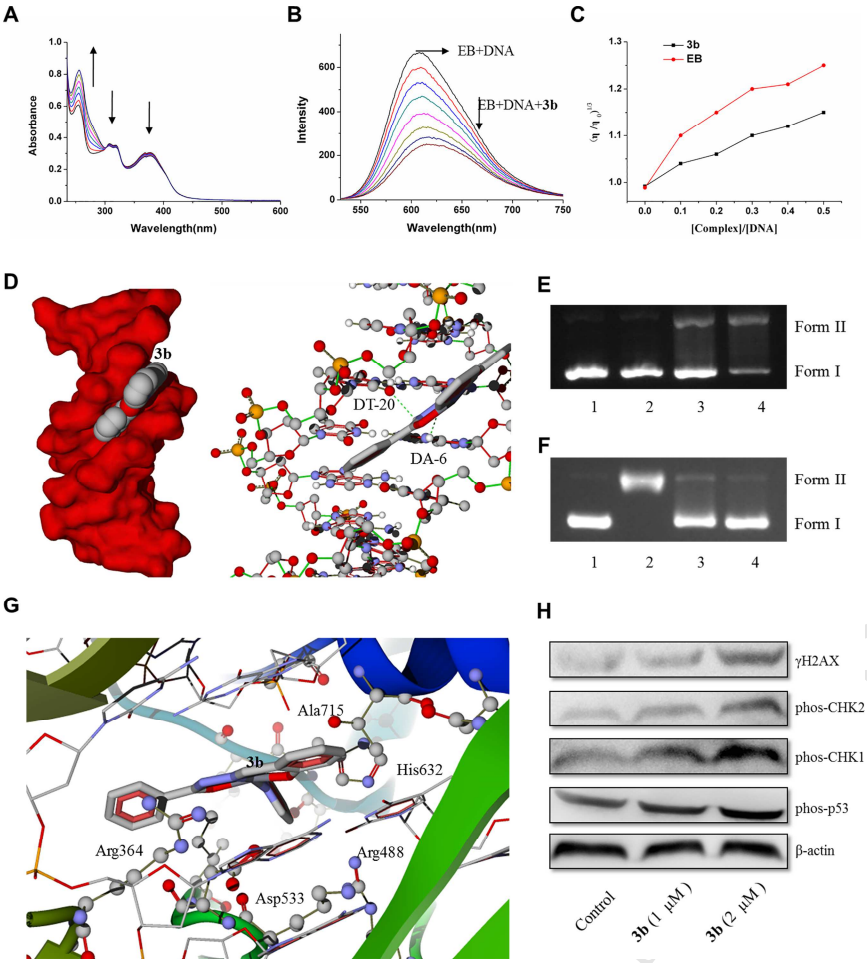

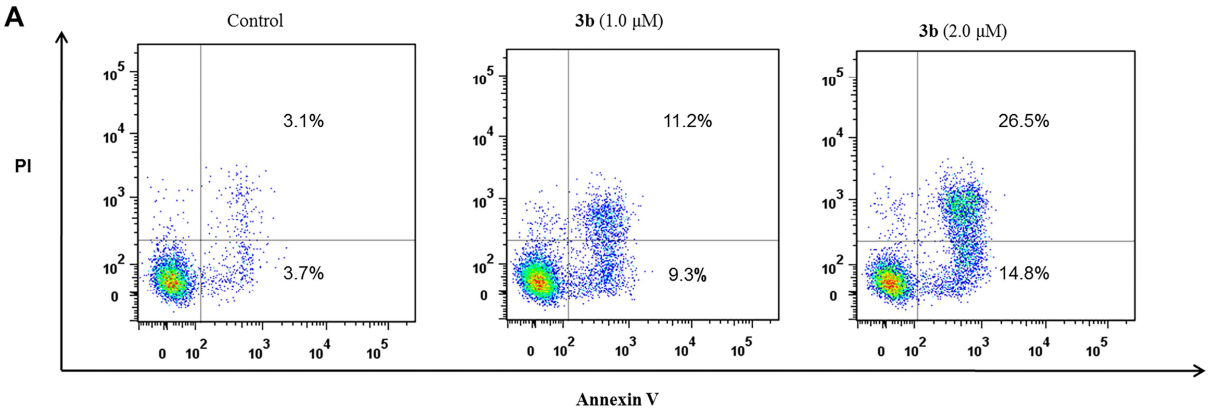

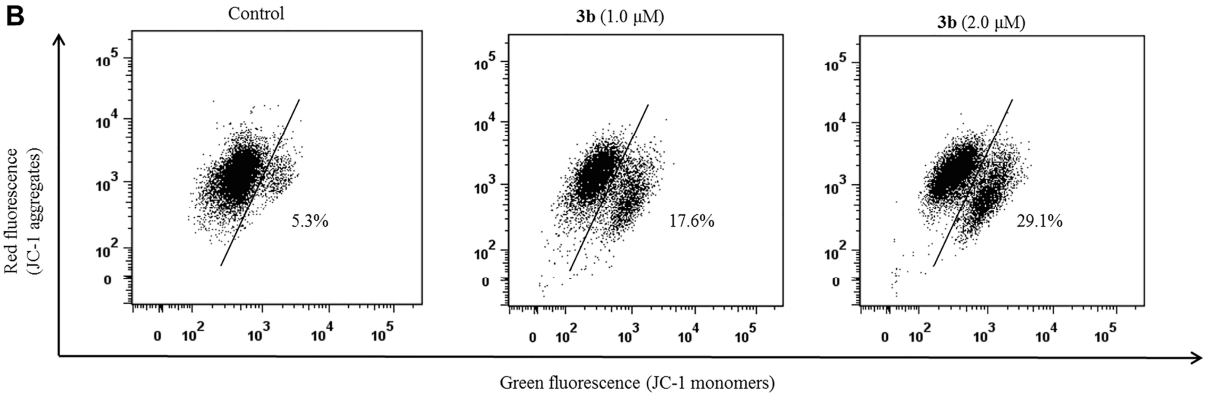

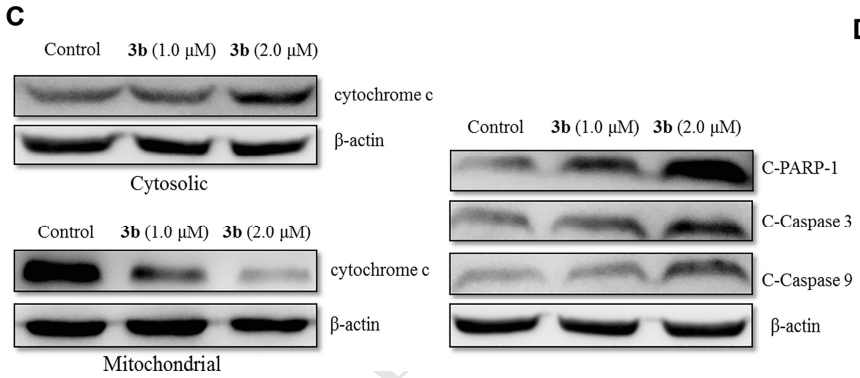

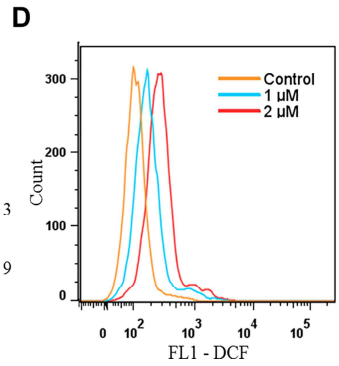

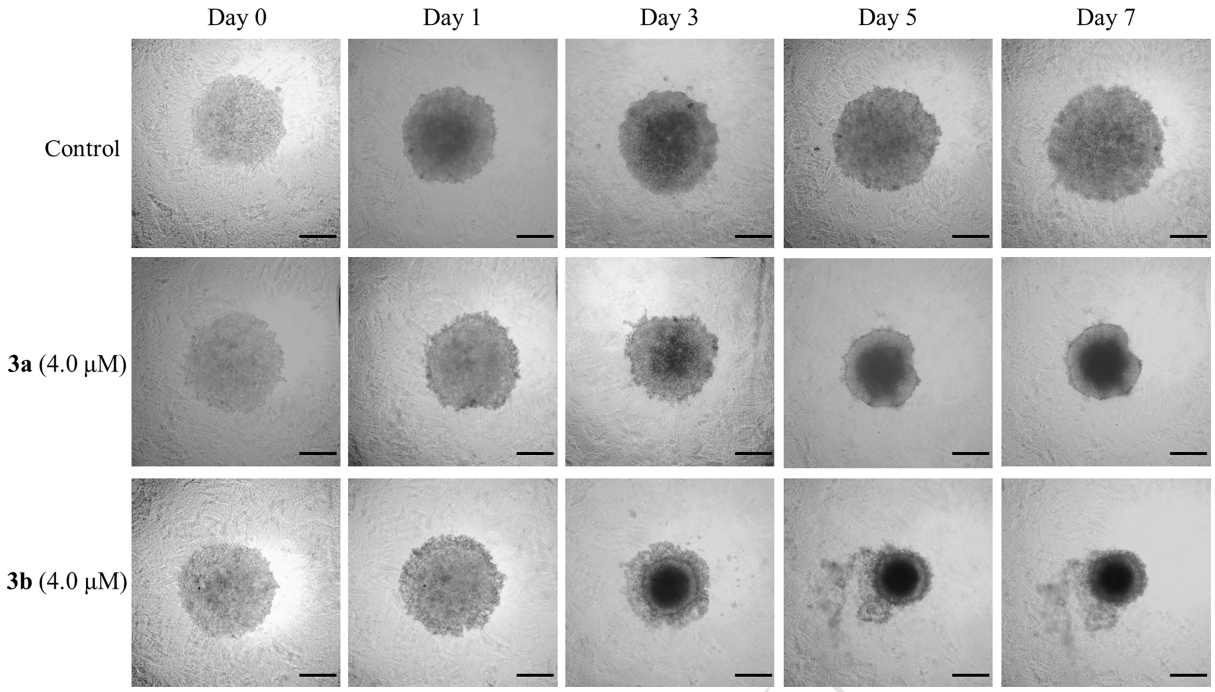

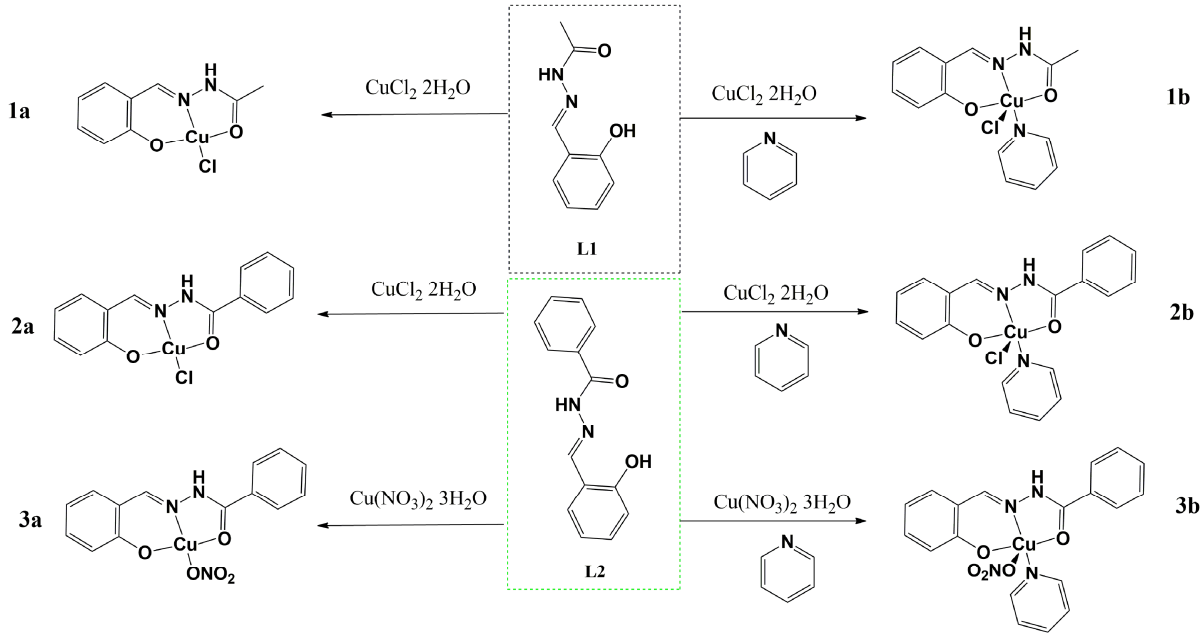

Highlights

- We have synthesis of the 1:1:1 Cu(II)/ligand/co-ligand complexes.
- The 1:1:1 complex had better antitumor activity than the corresponding 1:1 complex.
- The **3b** complex was active in 3D culture model.
- We revealed the anticancer mechanism of the **3b** complex.